Ceramics International 44 (2018) 236–245

Contents lists available at ScienceDirect

Ceramics International

journal homepage: www.elsevier.com/locate/ceramint

Structural properties and self-activated photoluminescence emissions in hydroxyapatite with distinct particle shapes

Thales R. Machado[a], Júlio C. Sczancoski[a], Héctor Beltrán-Mir[b], Máximo S. Li[c], Juan Andrés[d], Eloisa Cordoncillo[b], Edson Leite[a], Elson Longo[a,*]

[a] CDMF-UFSCar, Universidade Federal de São Carlos, P.O. Box 676, 13565-905 São Carlos, São Paulo, Brazil
[b] QIO-UJI, Universitat Jaume I, 12071 Castellón, Spain
[c] IFSC-USP, Universidade de São Paulo, P.O. Box 369, 13560-970 São Carlos, São Paulo, Brazil
[d] QFA-UJI, Universitat Jaume I, 12071 Castellón, Spain

ARTICLE INFO

Keywords:
Hydroxyapatite
Chemical precipitation
Photoluminescence
Electronic structure
Defects
Order-disorder

ABSTRACT

The understanding on defect-related photoluminescence (PL) properties of hydroxyapatite (HA) particles has a fundamental importance in the technological field for the development of new non-toxic biomedical and optical devices. However, the mechanisms responsible for this intrinsic PL in HA are not completely elucidated in the literature yet. In the present paper, stoichiometric and calcium-deficient HA nano- and micro-particles were synthesized by chemical precipitation. The influence of structural and morphological features on the intrinsic PL and electronic structure of this material were investigated by varying the addition rate of the phosphate precursor (0.15, 7.00 or 600.00 mL/min) and pH (4.5–5.0 or 9.5–10.0) value adopted in the precipitation. The results indicated that the structural order at long- and short-range varied with the synthesis conditions and particle shapes (rods, needles, plates, and rices). The blue and green PL emissions were attributed to defects (bulk, surface and interface) in the samples. These defects promoted the formation of additional energy levels within the band gap, as revealed by using two distinct excitation wavelengths for photoemission measurements. The energies of these wavelengths (~ 3.54 and ~ 2.98 eV at 350 and 415 nm, respectively) were lower than the band gap energies of HA samples (from 5.59 to 5.72 eV). A general model was proposed to explain the occurrence of self-activated PL in HA structure.

1. Introduction

The development of new compounds with highly efficient and tunable optical properties has become increasingly challenging for industry. In special, scientists and engineers have focused significantly on investigating and optimizing inorganic solids that consist of luminescent centers. Various optical devices, such as fluorescent lamps, light-emitting diodes, luminescent pigments, and sensors, which are based on these systems, have been obtained [1–4]. In the biomedical field, fluorescent materials, such as metal chalcogenide quantum dots, noble metal particles, lanthanide-based materials, etc, are promising candidates for bioimaging and monitored drug delivery because of their intense, stable, and tunable emissions [5–8]. However, the production of luminescent materials composed of environmentally friendly and non-toxic particles remains challenging.

In the last few decades, apatite-type materials have been used as hosts for different luminescent centers, especially transition metals and lanthanides [9,10]. In particular, hydroxyapatite (HA) is typically doped with Eu^{3+} and Tb^{3+} for biomedical approaches, owing to the luminescence properties of these lanthanide elements, and the biocompatibility, drug-loading efficacy, and cell-internalization capability of the final material [11–18]. However, intense self-activated photoluminescence (PL) processes are expected in HA samples because of the presence of high densities of structural and superficial defects arising from chemical synthesis at low temperatures [19]. Previous studies have demonstrated the application of these HA systems as fluorescent agent for bioimaging and biolabeling [20,21], monitored drug delivery systems [22,23], white-light emitting diodes [24] and so on. Although less investigated than Ln^{3+}-doped HA and other fluorescent systems, HA with self-activated PL can be technologically advantageous in terms of cost, and non-toxicity; however, the mechanisms responsible for intrinsic PL in HA are not completely elucidated in the literature.

Stoichiometric HA [SHA, $Ca_{10}(PO_4)_6(OH)_2$] is composed of phosphate clusters ([PO_4]), typically forming a hexagonal crystal pattern that is described by space group $P6_3/m$ [25]. Ca species occupy distinct crystallographic sites in this structure, and the corresponding general

* Corresponding author.
E-mail address: elson.liec@gmail.com (E. Longo).

http://dx.doi.org/10.1016/j.ceramint.2017.09.164
Received 29 June 2017; Received in revised form 19 September 2017; Accepted 20 September 2017
Available online 21 September 2017

formula of SHA is given as $Ca(1)_4Ca(2)_6(PO_4)_6(OH)_2$. Ca(1) sites form columns on the ternary axes of the structure, which are surrounded by nine O atoms belonging to PO_4 tetrahedra, thereby resulting in $[CaO_9]$ clusters. Ca(2) sites are located at the corners of equilateral triangles and hence, form the hexagonal channels of the structure. These species are surrounded by six O atoms that comprise the $[PO_4]$ clusters and one OH group inside the channel, thereby leading to $[CaO_7H]$ clusters. The hexagonal character of the HA lattice can be retained, even in the presence of various ionic substitutions and vacancies [26–28]. This feature is also evidenced by the fact that HA exists in the non-stoichiometric, Ca-deficient form, which is typically represented as $Ca_{10-x}(HPO_4)_x(PO_4)_{6-x}(OH)_{2-x}$ $(0 < x < 1)$(Ca-dHA) [29]. Ca-dHA has distinct chemical properties compared to SHA; for example, its higher solubility leads to an increase in the bioresorption rate in vivo [30]. Moreover, vacancies in Ca-dHA lead to changes in the electronic structure and density of e'–$h^{\bullet}$ pairs [31] which, in turn, may affect the intrinsic PL emission.

Various mechanisms have been proposed in order to explain the intrinsic PL of HA [21,32,33]. However, the effect of the degree of structural order-disorder, chemical composition, and morphological features, on the self-activated PL and electronic structure of HA particles, remains unclear. Moreover, several synthesis methods have been employed to obtain HA [34]. One of these methods, chemical precipitation, can be used to obtain distinct particle shapes and introduce several types of defects into the structure, in order to understand its PL. Recently, our research group reported the effect of different heat treatment temperatures on the intrinsic PL of HA nanorods [35]. In the present study, SHA and Ca-dHA with distinct sizes and shapes were synthesized via chemical precipitation. The influence of pH and addition rate of phosphate precursor on the structural ordering (long- and short-range), morphological features, and PL properties of these materials were investigated in detail.

2. Experimental section

2.1. Materials and methodology

Calcium nitrate tetrahydrate $[Ca(NO_3)_2{\cdot}4H_2O]$ (99%, Sigma-Aldrich) and di-ammonium phosphate $[(NH_4)_2HPO_4]$ (98+%, Strem Chemicals) were used as starting precursors. The pH of the solutions was controlled by adding ammonium hydroxide $[NH_4OH]$ (ACS, Acros). *Milli-Q* water was used as the solvent. Two main groups were synthesized via chemical precipitation in a: (1) basic environment with addition of NH_4OH (pH_{final} = 9.5–10.0), and (2) acidic environment without addition of NH_4OH (pH_{final} = 4.5–5.0). Moreover, in order to obtain distinct particle shapes, the addition rate of the phosphate precursor in aqueous solutions containing Ca^{2+} ions, was varied. Table 1 lists the main experimental parameters. The samples were all synthesized at 90 °C.

Table 1
Experimental parameters employed in the chemical precipitation of HA.

Sample group	Sample label	Mixture method	Addition rate of phosphate precursor (mL/min)	pH_{final}
With addition of NH_4OH	BIP	Injection pump	0.15 (Slow)	9.5–10.0
	BPP	Peristaltic pump	7.00 (Moderate)	9.5–10.0
	BOB	One batch	600.00 (Rapid)	9.5–10.0
Without addition of NH_4OH	AIP	Injection pump	0.15 (Slow)	4.5–5.0
	APP	Peristaltic pump	7.00 (Moderate)	4.5–5.0
	AOB	One batch	600.00 (Fast)	4.5–5.0

2.2. Synthesis using injection pump

In this step, well-crystallized particles were obtained by slowly mixing the precursors using an injection pump. Firstly, 50 mL of an aqueous solution containing 1.0 mmol of Ca^{2+} ions, and 12 mL of an aqueous solution containing 0.6 mmol of the phosphate precursor were prepared; these were referred to as solution 1 and solution 2, respectively. In order to obtain the sample prepared in a basic environment, the pH of both solutions was adjusted to 9.5–10.0 by adding NH_4OH. The samples were prepared by adding solution 2 to solution 1, at an approximate addition rate of 0.15 mL/min. The mixture was then ripened for 2 h. The milky suspensions obtained were repeatedly washed with *Milli-Q* water and ethanol, and centrifuged (8000 rpm) in order to eliminate residual groups. The resulting powders were dried at 80 °C for 24 h under air atmosphere. The samples prepared with and without addition of NH_4OH were referred to as BIP (Basic – Injection Pump) and AIP (Acid – Injection Pump), respectively.

2.3. Synthesis using peristaltic pump

This synthetic route was based on our previous study published [35]. The experimental procedure was similar to that used for the synthesis via IP; however, the solutions were mixed at a moderate addition rate (7 mL/min) of phosphate precursor by using a peristaltic pump. Moreover, solutions 1 and 2 consist of 50 mL of aqueous solution containing 10 mmol of Ca^{2+} ions and 100 mL of aqueous solution containing 6 mmol of the phosphate precursor, respectively. The as-prepared samples were referred to as BPP (Basic – Peristaltic Pump) and APP (Acid – Peristaltic Pump).

2.4. Synthesis by one-batch step

This procedure was used to obtain poorly crystallized samples. The experimental parameters were similar to those described by the PP. The only difference adopted was the mixture of both solutions, which was performed by one-batch step; the addition rate of the precursor was ~ 600 mL/min. The as-prepared samples were referred to as BOB (Basic – One Batch) and AOP (Acid – One Batch).

2.5. Characterization

The chemical composition of the prepared samples was determined via inductively coupled plasma-atomic emission spectrometry (ICP-AES) using a Thermo Scientific iCAP 6500 (USA) analyzer. The samples were structurally characterized by X-ray diffraction (XRD) in a Shimadzu XRD–6000 (Japan) diffractometer using *Cu-Kα* radiation (λ = 0.154184 nm). Data were collected over 2θ ranging from 20° to 70°, and at a step scan rate and step size of 0.2°/min and 0.02°, respectively. The peak broadening of the reflection was used to determine the crystallographic domain size (*Xs*) of the samples, from the Scherrer equation [36]:

$$X_S = \frac{0.9 \times \lambda}{\beta \times \cos\theta} \tag{1}$$

where λ is the wavelength of the x-rays and θ is the Bragg angle of the analyzed peak; β is the line broadening and is estimated from:

$$\beta = \sqrt{\beta^2_{\text{observed}} - \beta^2_{\text{instrumental}}} \tag{2}$$

where $\beta_{observed}$ is the observed broadening, as determined from the full width at half maximum (FWHM), and $\beta_{instrumental}$ is the instrumental broadening, as determined from FWHM of a well-crystallized SiO_2 (quartz) external standard. In HA samples, *Xs* along perpendicular directions can be estimated by using the (002) and (300) diffraction peaks; this estimation is based on the assumption that the typical crystal growth (i.e., along *c* planes) occurs and the length of the crystal

corresponds to the *a* planes [37].

The morphological features were examined by using a field-emission scanning electron microscope (FE-SEM) in a Carl Zeiss Supra 35-VP (Germany) microscope operated at 5 kV. Fourier transform infrared spectroscopy (FTIR) was performed at room temperature using a Jasco FT/IR–6200 (Japan) spectrophotometer operated in absorbance mode. Spectra were recorded at a resolution of 4 cm^{-1}, over wavenumbers ranging from 400 to 4000 cm^{-1}. These measurements were performed on 12-mm-diameter pellets, which were composed of 1 wt% of each sample mixed with 99 wt% of KBr (≥ 99%, Sigma-Aldrich). Micro-Raman spectroscopy was performed by using a Horiba Jobin-Yvon IHR550 (Japan) spectrometer coupled to a CCD detector and a Melles Griot argon-ion laser (USA), operated at 514.5 nm with maximum power of 200 mW. UV–vis spectroscopy was performed by using a Varian Cary 5G (USA) spectrophotometer operated in diffuse-reflection mode. PL spectroscopy was conducted at room temperature by using a Thermal Jarrel Ash Monospec 27 (USA) monochromator coupled to a Hamamatsu R955 (Japan) photomultiplier. A Coherent Innova 200 K krypton ion laser (USA) (λ_{exc} = 350 and 415 nm) was used as an excitation source. These two excitation wavelengths were used to reveal the band structures in HA samples. The incident laser beam on each sample was maintained at a maximum power of 15 and 7 mW, respectively.

3. Results and discussion

3.1. Composition and structural analyses of prepared samples

The composition of HA samples is strongly dependent on the synthesis conditions, and these samples may exist as either SHA (Ca/P = 1.67) or Ca-dHA (1.50 ≤ Ca/P < 1.67) [38]. Table 2 shows the chemical composition, as determined via ICP-AES. As can be seen, the Ca/P ratios of samples synthesized in a basic environment (BIP, BPP, and BOB) are similar to those of SHA. The Ca/P ratios of the samples synthesized without NH_4OH (AIP, APP, and AOB) are similar to those of Ca-dHA. These results confirm that the experimental methodology employed in our study is effective in preparing SHA and Ca-dHA samples.

The occurrence of HA as a single phase, or simultaneously with other orthophosphate phases, is also strongly dependent on the synthesis parameters [39]. Fig. 1(a) and (b) shows XRD patterns of the prepared samples. The diffraction peaks can all be perfectly assigned to the pure hexagonal HA phase (space group $P6_3/m$), in good agreement with the results reported in Inorganic Crystal Structure Data (ICSD) base No. 26204 [25]. It is important to emphasize that HA lattice can accommodate high densities of vacancies without undergoing significant structural changes. Therefore, both Ca-dHA and SHA structures have similar XRD patterns.

The XRD peaks of both groups (with and without the presence of NH_4OH) narrowed, in general, with decreasing addition rate of the phosphate source. This indicates that the size and degree of long-range ordering of the particles depend on the rate of addition. As such, the samples prepared by injection pump (BIP and AIP) exhibit a higher degree of crystallization or periodicity in the lattice than the other samples. This structural behavior is also manifested as changes in the

Table 2
Composition of the as-prepared samples as determined via ICP-AES.

Sample	Ca (%m/m)	P (%m/m)	Ca/P
BIP	31.30	18.60	1.68
BPP	34.40	20.61	1.67
BOB	34.80	20.81	1.67
AIP	32.90	20.31	1.62
APP	32.60	21.00	1.55
AOB	31.10	19.30	1.61

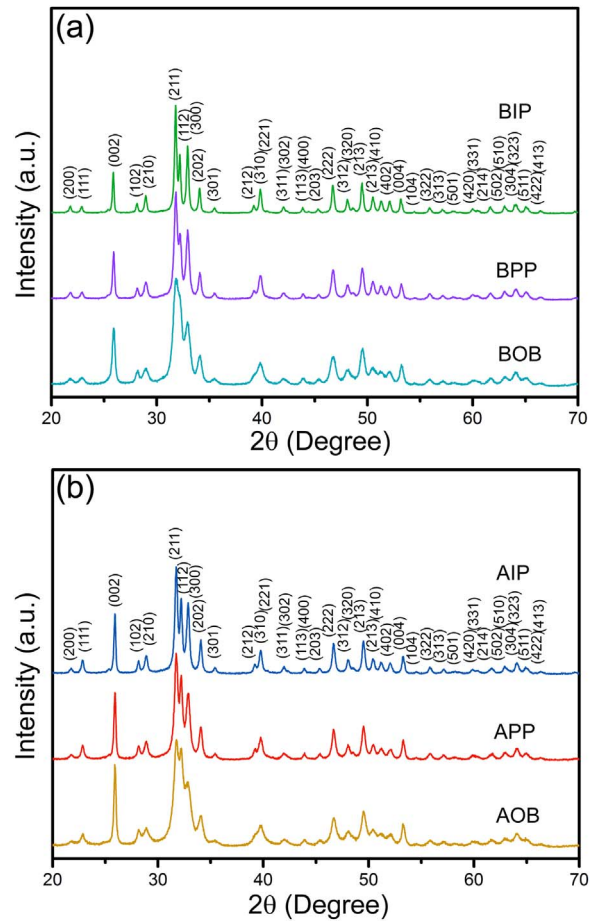

Fig. 1. XRD patterns of samples obtained at different addition rates of the phosphate source, for (a) pH_{final} = 9.5–10.0 and (b) pH_{final} = 4.5–5.0.

Table 3
Xs values of distinct crystallographic orientations of the as-prepared samples.

Addition rate	With addition of NH_4OH			Without addition of NH_4OH		
	$Xs_{(002)}$ (nm)	$Xs_{(300)}$ (nm)	$Xs_{(002)}$ / $Xs_{(300)}$	$Xs_{(002)}$ (nm)	$Xs_{(300)}$ (nm)	$Xs_{(002)}$ / $Xs_{(300)}$
Slow	58.75	40.69	1.44	52.85	27.82	1.89
Moderate	44.14	24.80	1.78	44.61	19.80	2.25
Fast	36.57	15.02	2.36	39.78	11.49	3.46

Ca–O and P–O bond lengths of [CaO_9], [CaO_7H], and [PO_4] clusters, respectively, in both groups of samples.

The crystalline nature of these samples was investigated via the crystallographic coherence domain sizes (*Xs*). Table 3 shows *Xs* the values (estimated from Eq. (1)) associated with the (002) and (300) crystallographic planes, and the corresponding (002)/(300) aspect ratio. Values ranging from 36.57 to 58.75 nm and from 15.02 to 40.69 nm for the (002) and (300) planes, respectively, confirm the presence of nanocrystalline HA. Moreover, in both cases, slow rates of addition yield larger domains than high rates. Analysis of the (002)/(300) ratios reveals that SHA obtained in a basic environment crystallizes anisotropically along crystallographic direction *c*. Similar *Xs* behaviors were observed for the Ca-dHA samples prepared in an acidic environment. However, this group consisted of more anisotropic domains than the group obtained in a basic environment.

FTIR and Raman spectroscopies of solids can also be used to identify phases and reveal the short-range ordering in materials [40]. According to experimental and theoretical data, the SHA unit cell (whose

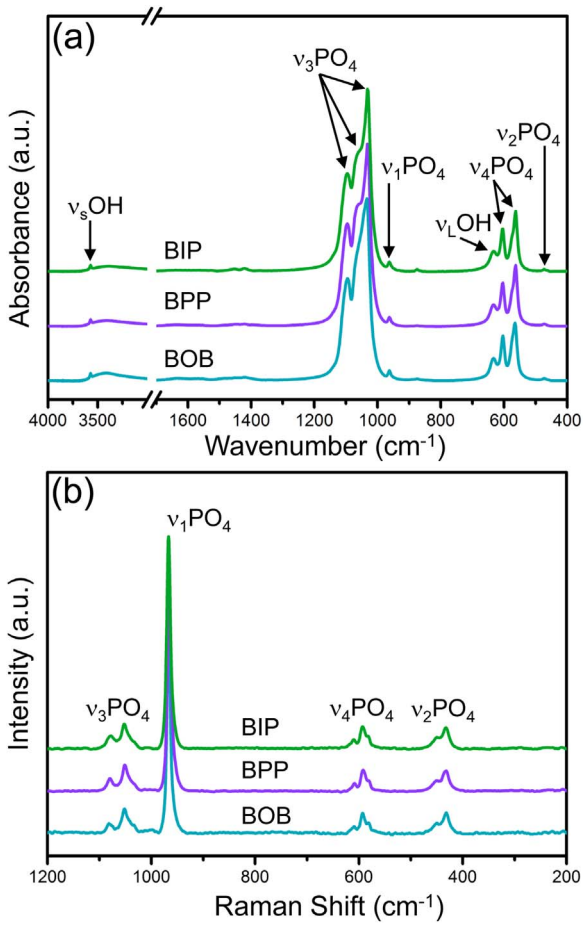

Fig. 2. (a) FTIR and (b) Raman spectra of as-prepared samples obtained in a basic environment (pH_{final} = 9.5–10.0), at different addition rates of the phosphate source.

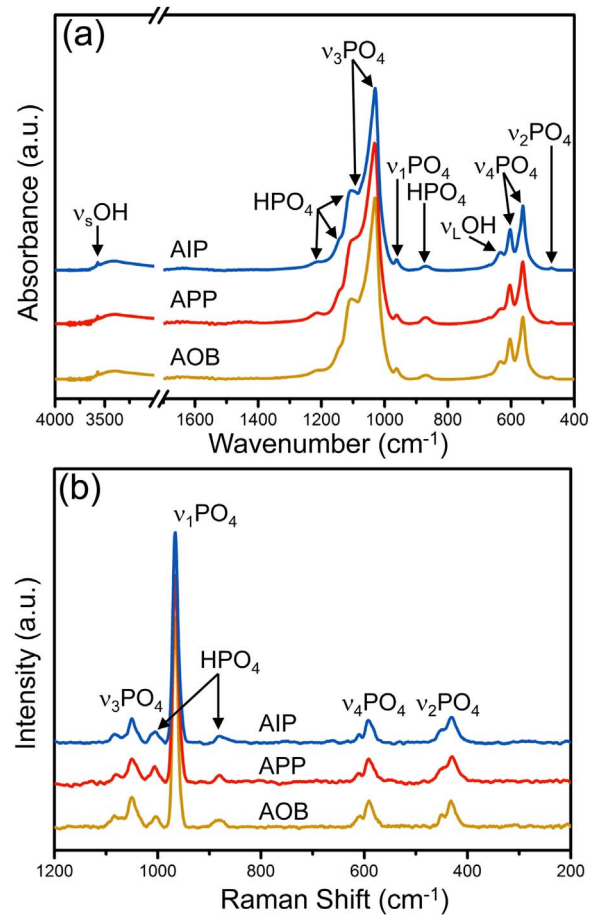

Fig. 3. (a) FTIR and (b) Raman spectra of as-prepared samples obtained without addition of NH_4OH (pH_{final} = 4.5–5.0) and at different addition rates of the phosphate source.

symmetry is described by space group $P6_3/m$ (C_{6h})) is composed of 44 atoms, which yield 132 internal and lattice modes [41,42]. Most of the active modes give rise to bands in the FTIR and Raman spectra of SHA, which correspond to librational and stretching modes of OH groups and internal vibrations of $[PO_4]$ clusters [43,44].

Fig. 2(a) and (b) shows the FTIR and Raman spectra of samples precipitated in a basic environment (pH_{final} = 9.5–10.0); the main modes are listed in Table S1. The detected bands are characteristic of SHA samples [41,44]. In other words, the bands associated with the ν_1 symmetric and ν_3 asymmetric stretching modes of $[PO_4]$ clusters, as well as the ν_2 and ν_4 bending modes, were all identified. Bands corresponding to OH librational and symmetric stretching vibrations were also present in all the spectra.

The bandwidth of the vibrational spectrum has been used to determine the degree of short-range ordering in HA [45]. In this study, the samples prepared in a basic environment exhibit relatively well-defined FTIR and Raman-active bands, which are indicative of short-range structural ordering. Several bands, corresponding to the ν_3 stretching vibration of $[PO_4]$ clusters, occur at wavenumbers from 1000 to 1100 cm^{-1}, and the differences between the samples are especially noticeable in this range. The samples may be written as BOB < BPP ≈ BIP, i.e., in ascending order of the sharpness of the bands in the FTIR spectra. Therefore, in a basic environment, rapid addition rates of the phosphate precursor lead to poor crystallization of the HA samples and hence, low degree of short-range ordering of $[PO_4]$ clusters in the lattice.

Fig. 3(a) and (b) shows FTIR and Raman spectra collected from samples synthesized in an acidic environment (pH_{final} = 4.5–5.0). Active bands, which correspond to Ca-dHA, occur in both spectra [29]. The identified bands and their respective vibrational modes are all listed in Table S2. The bands associated to $[PO_4]$ clusters (ν_3PO_4 → FTIR; ν_4PO_4 → Raman) in Ca-dHA samples prepared in an acidic environment were less resolved than those of the samples prepared in a basic environment. This behavior is attributed to changes in the local symmetry and/or increased disorder in HA [45,46]. Moreover, the intensity of the bands associated with O–H bonds (ν_LOH → FTIR) decreased in the FTIR spectra, and the vibrational modes arising from the protonation of $[PO_4]$ clusters (HPO_4 in Fig. 3(a) and (b)) occurred in both spectra [47]. These results confirm that Ca-dHA is formed under the present synthesis conditions, with Ca ionic vacancies (V_{Ca}) maintaining the electroneutrality of the structure. Therefore, the pH and addition rate of phosphate both play a key role in the formation and organization processes of $[CaO_9]$, $[CaO_7H]$ and $[PO_4]$ clusters in the hexagonal HA structure.

3.2. Morphological analysis

Fig. 4(a)–(c) shows FE-SEM micrographs of samples prepared in the basic environment. As Fig. 4(a) shows, the BIP sample is composed of several hexagonal prism-like microparticles. Increasing rates of addition of the phosphate precursor resulted, however, in a reduction in the particles sizes and changes in their shapes. BPP and BOB samples are formed by rod-like microparticles and rice-like nanoparticles, respectively (Fig. 4(b) and (c)). The dimensions of the particles are listed in Table 4.

Fig. 4(d)–(f) shows FE-SEM micrographs of the as-prepared samples without the addition of NH_4OH. As in the case of the samples prepared in a basic environment, the particle sizes decreased with increasing

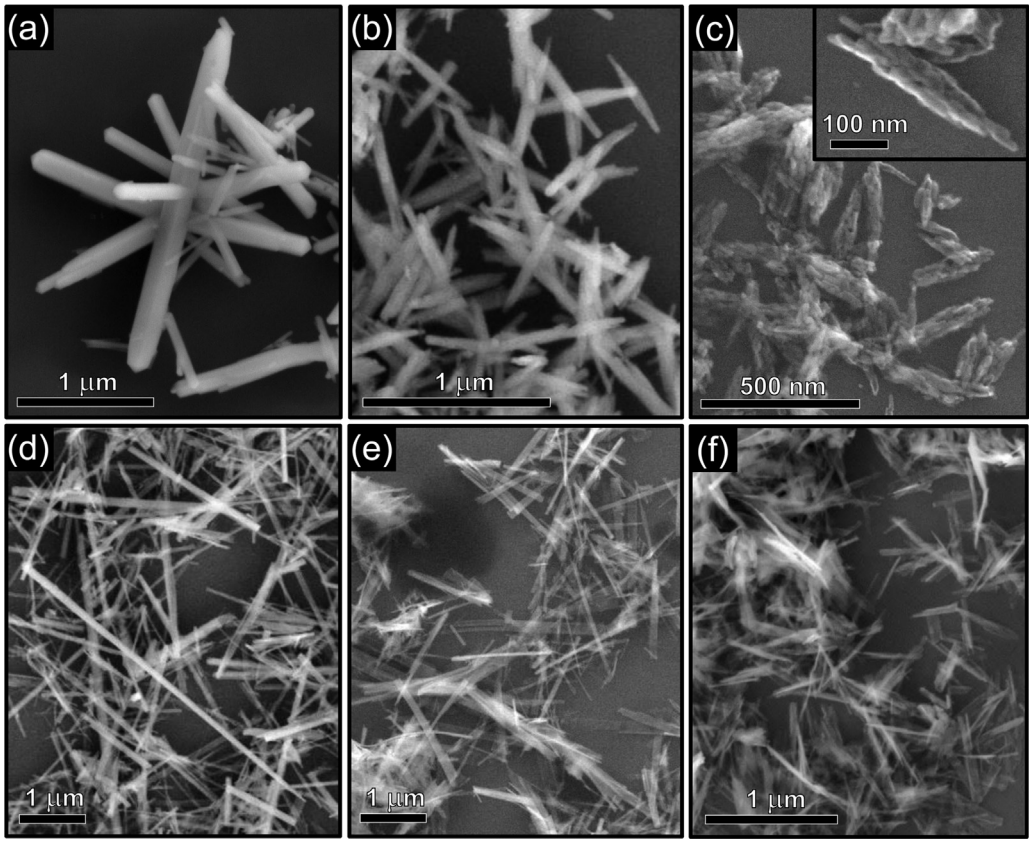

Fig. 4. FE-SEM micrographs of samples prepared at pH_{final} = 9.5–10.0 [(a) BIP (injection pump), (b) BPP (peristaltic pump), and (c) BOB (one-batch addition)], and at pH_{final} = 4.5–5.0 [(d) AIP (injection pump), (e) APP (peristaltic pump), and (f) AOB (one-batch addition)].

Table 4
Shapes and approximate size of particles in the HA samples.

Sample	Shape	Length (μm)	Width (nm)
BIP	Hexagonal prism	0.7–2.5	70–200
BPP	Rod	0.3–0.6	40–80
BOB	Rice	0.05–0.06	12–25
AIP	Plate and needle	0.5–5.5	30–200
APP	Plate and needle	0.5–3.5	30–200
AOB	Needle	0.2–0.7	20–50

addition rate of the phosphate source. The AIP (Fig. 4(d)) and APP (Fig. 4(e)) samples are composed of needle- and plate-like microparticles, respectively. The particles in APP samples are, however, smaller than the particles in AIP sample. The AOB sample (Fig. 4(f)) prepared by one-batch step is composed of needle-like microparticles. These particles are the smallest of all particles formed in this group of samples. As Table 4 shows, for the same rate of phosphate addition, the samples prepared without NH_4OH undergo more anisotropic crystallization than those prepared in a basic environment, corroborating with *Xs* estimations in this work.

3.3. Formation mechanisms of SHA and Ca-dHA particles

During synthesis under alkaline conditions, SHA is the most thermodynamically stable phase [48], owing to the significant concentration of deprotonated PO_4^{3-} and OH^- ions in the solution. However, amorphous Ca phosphate will precipitate first and is then slowly converted to Ca-dHA. This temperature-dependent stage is critical for the formation of SHA. In the case of chemical synthesis performed at room temperature, Ca-dHA is formed after only several hours. At temperatures above 90 °C, however, this phase crystallizes almost instantaneously, although an aging step is still required for the transition from Ca-dHA to SHA [49,50]. In our reactions performed at 90 °C (basic conditions), 2 h of aging were needed to convert Ca-dHA to SHA, even in samples prepared at a rapid rate of phosphate addition. The crystal shape and size constitute main differences among the samples. Therefore, the particle shape and size depend on the method of addition, indicating that this parameter plays a key role in the nucleation and growth processes. The BIP sample exhibited a good degree of long-range structural ordering and the corresponding particles have similar shapes to those that comprise the hexagonal HA structure [37]. In this case, the addition of the phosphate precursor (by means of an injection pump) resulted in a low nucleation rate and hence, a dominant growth stage. During this synthesis, drops containing PO_4^{3-} ions fall into a saturated solution that consist of Ca^{2+} ions, and nucleation is thereby initiated. The precursor ions also can gradually accumulate on the surface of the previously formed nanocrystals in the solution, resulting in the growth of hexagonal prism-like microparticles. In addition, the growth process of these microstructures is controlled by oriented attachment between the nanocrystals followed by Ostwald ripening [51], when the system has reached an equilibrium condition. Hence, the self-assembly is a common phenomenon in laboratory and physiological systems for HA samples [52,53], such as the complex hierarchical structure on tooth enamel [54].

The crystal growth mechanism that operates in the BIP sample may also takes place in the BPP sample that was prepared at a slightly higher addition rate of phosphate by using a peristaltic pump. However, this slightly higher rate resulted in a change in the crystal shape (i.e., to rod-like microparticles), indicating that nucleation dynamics have significant effect on the subsequent growth stages. On the other hand, in the case of the BOB sample, a high density of crystallization nuclei is formed, owing to abrupt precipitation and high supersaturation. This formation leads, in turn, to the formation of several rice-like nanoparticles. Spontaneous collisions and mutual interactions (via oriented attachment) between these nanoparticles, result in the formation of complex structures (self-assembly of nanoparticles). Moreover, the formation of HA lattice, via rapid Coulomb interactions between PO_4^{3-}

and Ca^{2+} ions, leads to long- and short-range (albeit slight) structural disorder, as evidenced by XRD patterns and vibrational spectroscopies, respectively.

For samples prepared without the addition of NH_4OH, the acidic environment provided the ideal kinetic condition for the formation of other intermediary phosphate phases, which nucleate first in the aqueous system. Synthesis of SHA is difficult in this environment, and Ca-dHA is the only final product obtained. The plate-shaped particles and the $[PO_4H]$ that comprise the AIP, APP, and AOB samples indicate, therefore, that octacalcium phosphate (OCP, $Ca_8(HPO_4)_2(PO_4)_4{\cdot}5H_2O$, Ca/P = 1.33) may have precipitated prior to Ca-dHA [55]. In principle, OCP hydrolyses to Ca-dHA in aqueous solutions, in which $[PO_4H]$ deprotonation occurs. One of the two crystallographically non-equivalent $[PO_4H]$ clusters, present in OCP, may maintain the protonation character [47]. The XRD, FTIR, and Raman results confirmed that OCP transitioned to the Ca-dHA phase. This interpretation is supported by ICP-AES data, which revealed that the Ca/P ratios correspond to different stoichiometry from that of OCP (Table 2).

OCP crystallizes to a triclinic structure, whose symmetry is described by the space group *P*1; this structure consists of alternating apatite-like layers and hydrated layers parallel to the (100) plane [56]. The faces of the OCP crystals, corresponding to these planes, are more hydrated than other faces and hence, the adhesion of Ca^{2+} and $H_xPO_4^{x-3}$ is prevented. Therefore, crystals tend to growth in *c-axis*, and (100) faces are predominant in the final crystal shape. There are two (100) faces in OCP, which lead to growth of plate-like particles [57]. Morphological aspects may be retained after transition to Ca-dHA, as evidenced by the shape of the nanoparticles obtained in an acidic environment. The difference in size and ordering of the species in Ca-dHA particles of AIP, APP, and AOB samples is attributed to similar factors cited for samples synthesized in a basic environment. The rapid addition of phosphate precursor (AOB) leads to an increase in the nucleation rate and a decrease in the time allowed for accommodation of the species in the structure. However, the growth step is dominant in samples obtained by using a peristaltic pump (APP) and an injection pump (AIP), and therefore these samples accommodate the species more efficiently than their AOB counterpart.

A schematic of all the samples obtained in the present study is shown in Fig. 5. The particle shapes are shown compared with those revealed in the FE-SEM images of each sample. Moreover, a magnified view of the main diffraction peaks indicates that the peaks narrow, in general, with increasing crystallization of the samples.

3.4. Photoluminescence and electronic structure

The spontaneous formation of donor and acceptor levels within the band gap (lattice polarization), which are responsible for radiative and non-radiative transitions involving e'–$h^{\bullet}$ pairs, may be induced by the presence of defects. These defects include vacancies, dislocations, stresses and strains in the crystalline lattice, stacking faults, twin boundaries, distortions in the atomic bonds, cracks, pores, etc [58,59]. The factors that lead to the formation of these defects in solid matrices vary with the synthesis and processing technique used in the preparation of materials. Experimental parameters, such as sample type (powder, thin film, pellet), pressure, temperature, time, reaction medium (solid or liquid), atmosphere, etc., also have an effect on defect formation [60]. Therefore, control of the types and total density of defects formed in a material is difficult.

Defects related to the loss of symmetry in $[CaO_9]$, $[CaO_7H]$ and $[PO_4]$ clusters may exist in HA, owing to synthesis in an aqueous solution at relative low temperatures [30]. The loss of symmetry results possibly from the presence of V_{Ca} in the Ca clusters. This is expected since Ca species are loosely arranged in the lattice and have significant mobility [29,61,62]. In this study, V_{Ca} in the Ca-dHA samples (AIP, APP, and AOB) obtained in acidic environments, result from the absence of some Ca atoms from their respective sites in the apatite structure (ionic vacancy). V_{Ca} may have also originated from displacement of Ca species from their equilibrium positions (interstitial vacancy). These interstitial vacancies stem mainly from the poor arrangement of HA species in the lattice, owing to the crystallization process. In our samples synthesized in a basic environment, V_{Ca} interstitial vacancies are more easily formed than V_{Ca} ionic vacancies because of the synthesis conditions (especially in the case of the BOB sample) and the low density of protonated $[PO_4]$ clusters. These interstitial vacancies may also form in both studied groups, owing to distortions resulting from neighboring vacancies, such as those in hydroxyl groups [61,63]. $[PO_4]$ clusters are more stable than Ca clusters, and define the hexagonal HA structure, but may be distorted (symmetry loss) in the lattice. This distortion stems from changes in the P–O bond lengths and O–P–O bond angles; these changes are induced by the protonation in Ca-dHA [29] or long- and short-range structural disorder, and are manifested in the XRD (Fig. 1(a) and (b)), FTIR and Raman spectra (Figs. 2(a) and (b) and 3(a) and (b)). Considering these situations, we propose a model (see Fig. 6) based on the Kröger-Vink notation [64] to clarify the influence of V_{Ca} and disordered $[PO_4]$ clusters on the polarization process of the HA lattice. The $[PO_4]$, $[CaO_9]$, and $[CaO_7H]$ clusters shown in Fig. 6(a) are considered ideal (i.e., defect-free). Ionic and interstitial vacancies in both basic and acidic environments are denoted in Fig. 6(b)–(d). In these figures, $[V_{Ca}^{x}\,O_9]$ and $[V_{Ca}^{x}\,O_7H]$ are neutral Ca vacancies; $[V'_{Ca}O_9]$ and $[V'_{Ca}O_9H]$ are Ca vacancies that received one electron; $[V''_{Ca}O_9]$ is a Ca vacancy that received two electrons; $[PO_4]_d^x$ and $[PO_4]_d^{\bullet}$ are distorted/disordered phosphate clusters, where x and • denote a neutral state and a cluster with one hole (positive charge), respectively. These equations summarize the polarization effects resulting from the formation of vacancies, in which there is a charge transfer from perturbed to unperturbed clusters (structural order-disorder), i.e., formation of e'–$h^{\bullet}$ pairs [65]. For example, electronic transference from the $[PO_4]_d^{\bullet}$ cluster (perturbed) to the $[V''_{Ca}O_9]$ cluster (unperturbed).

In addition to the V_{Ca} and $[PO_4]$ distortions that are characteristic of the bulk and surface, other superficial and interfacial defects, such as grain boundaries, pores, cracks, etc., also occur in HA [66]. In principle, independent of the kinds of defects, they are able to promote a non-homogeneous charge distribution, as a consequence of the symmetry break induced by the delocalization of electronic densities associated with $[CaO_9]$, $[CaO_7H]$ and $[PO_4]$ clusters. Additional energy levels may occur within the forbidden zone or band gap, owing to this phenomenon [31,61,63]. Therefore, the band structure in HA samples may be revealed by combining the results of UV–vis measurements with PL spectra.

Fig. 7 shows the UV–vis spectra of the as-prepared samples. The linear portion (i.e., the tail) of these spectra was extrapolated, by using the modified Kubelka-Munk equation [67] (adopting n = 1/2 for indirect transitions [68]) to estimate the band gap energies (E_g) of each sample. The samples all presented high E_g values (from 5.59 to 5.72 eV), which are similar to those reported for HA [12,68]. The E_g of the as-prepared samples varied only modestly with the synthesis parameters. However, the lowest E_g of the BOB sample (~ 5.59 eV) suggests that this sample has the highest density of intermediary energy levels within the forbidden zone; these levels results from several types of defects (structural, surface and interface).

The influence of some parameters on the PL of HA, has been previously investigated. Zhang et al. [33] reported that impurity carbon dioxide radical anions ($CO_2^{\bullet-}$), located in the interstitial sites of the HA lattice, have a significant effect on the self-activated PL. Deshmukh et al. [21] described that discrete energy levels, arising from electrons trapped on the surface of HA nanorods, are able to improve the intrinsic PL of this material. Bystrova et al. [32] correlated experimental data and theoretical calculations, in order to explain the role of defects, in the organization of the band structure and PL activity of HA crystals; defects such as OH vacancies and H internodes were considered in that study. Recently, our research group experimentally demonstrated a

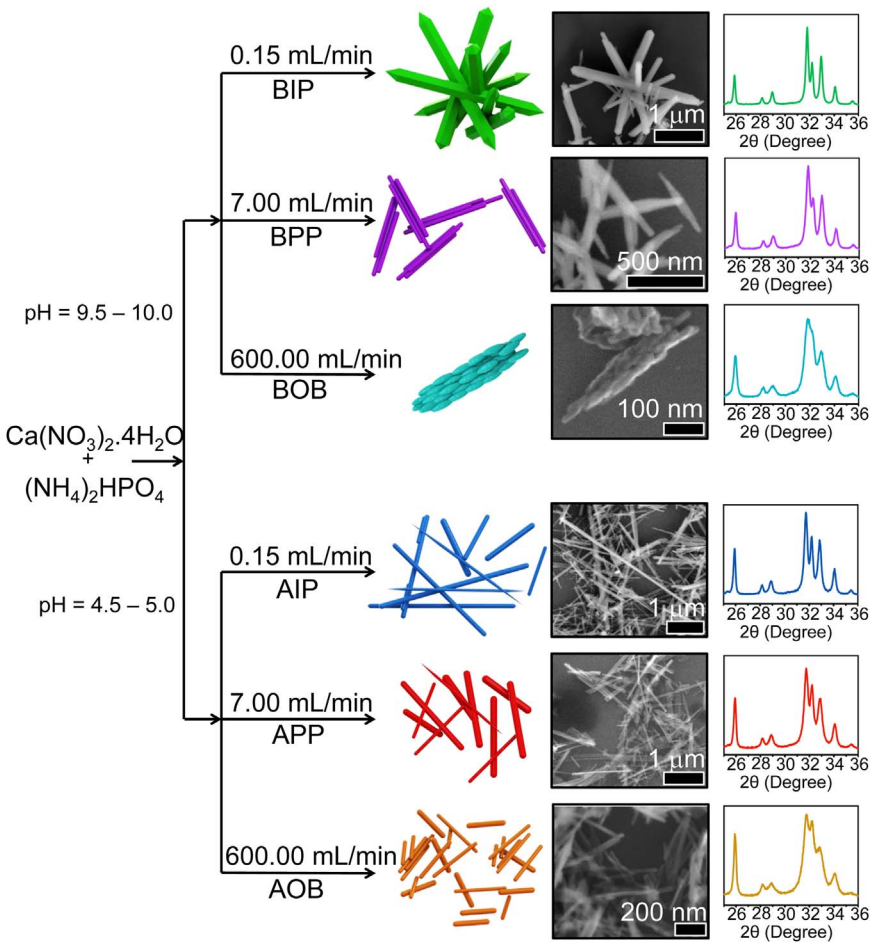

Fig. 5. Schematic of the experimental conditions, final particle shapes, and XRD patterns obtained in the present study.

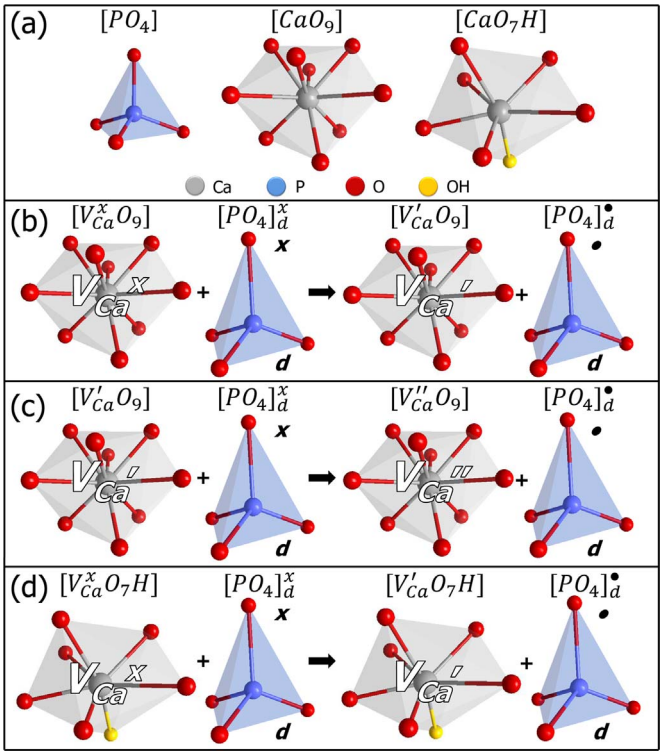

Fig. 6. Model based on the Kröger-Vink notation for the polarization process of the HA lattice: (a) ordered clusters of the HA structure, (b–d) formation mechanisms of Ca vacancies.

critical role of distinct defects, including entrapped impurities (H_2O, NH_4^+, HA…H^+, and CO_3^{2-}) and OH vacancies, on the structural order-disorder and intrinsic PL of heat treated HA samples (from 200 to 800 °C) [35]. In the present study, behind the pH value, it was experimentally investigated the effect of the addition rate of phosphate precursor and the distinct particle shapes as well as the formation of defects, for example, ionic and interstitial V_{Ca} vacancies, and distortions in $[PO_4]$ clusters on the PL response of our as-prepared HA samples.

Fig. 8(a) and (b) shows the PL spectra obtained at room temperature (from all samples) and at excitation wavelengths of 350 and 415 nm. These spectra have a broad profile, indicating that the emissions cover a large part of the visible electromagnetic spectrum. In this case, countless energy states are involving in the electronic transitions. As the UV–vis spectra (Fig. 7) showed, the E_g values (from 5.59 to 5.72 eV) of the samples are all higher than the excitation energies (~ 3.54 and ~ 2.98 eV at 350 and 415 nm, respectively). This indicates that band-to-band electronic transitions have negligible influence on the final PL. The explanation for this optical phenomenon is attributed to the occurrence of additional energy levels within the forbidden zone; these levels arise from interface, surface and bulk defects. In previous studies [69], additional levels were attributed to bulk and surface energy states, reinforcing the present interpretation. Moreover, these energy states are referred to as deep- or shallow-level defect states [70]. The deep levels occur near the middle of the band gap and give rise to green, yellow, orange, and red PL emission at room temperature. On the other hand, the shallow levels occur near the edge of the conduction band (CB) and/or valence band (VB). Those located near the CB edge play a crucial role in violet and blue PL emissions [71]. The maximum intensities in the PL spectra of the SHA and Ca-dHA samples (Fig. 8(a) and (b)) occur at wavelengths between 440 and 540 nm, which correspond

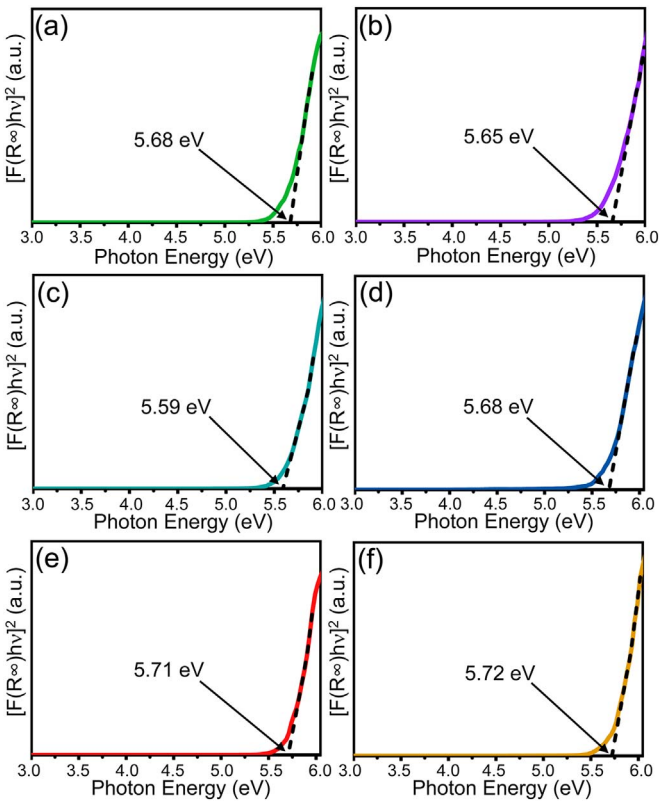

Fig. 7. UV–vis spectra of the samples synthesized in the present study: (a) BIP, (b) BPP, (c) BOB, (d) AIP, (e) APP, and (f) AOB.

to blue/green regions of the visible electromagnetic spectrum. Therefore, the observed emissions encompass both shallow- and deep-level defect states.

The spectra have similar profiles, although the emission intensities are different. These differences result from variations in the concentration of defects located mainly in the bulk (ionic and interstitial V_{Ca}, and distortions in $[PO_4]$ clusters). However, compared to those of Ca-dHA samples, PL spectra of SHA samples (especially the BOB sample) were slightly shifted toward higher wavelengths, irrespective of the excitation energy employed, as shown in Fig. 9(a)–(d). This shift is attributed to the effect of interface and surface defects. Moreover, rapid supersaturation occurs and several stable nuclei are formed, with increasing addition rate of the phosphate precursor. In the sequence, these nuclei interact, forming the nanoparticles. This process occurs very rapidly, thereby resulting in a high density of irregularities or defects (such as cracks, broken bonds, distortions in the $[PO_4]$ clusters, and V_{Ca}) on the surface of these nanoparticles. In addition, HA nanoparticles can rotate and/or collide with each other along the same crystallographic orientation (oriented attachment). Defects are formed in the interface region between the nanoparticles, in the case of an imperfect attachment [72].

As shown in previous sections, intrinsic defects have a significant impact on the electronic recombination mechanisms. The PL spectra (collected at both excitation wavelengths) were therefore deconvoluted, in order to determine (qualitatively) the contribution of each component or visible-light emission center; this deconvolution was performed by using the *PeakFit* software (4.05version), and the results are shown in Figs. S1 and S2. The PL profiles were all well-described by the Voigt area function; five components were needed for the spectra collected at an excitation wavelength of 350 nm, whereas six were required for those obtained at 415 nm. These components remained in the same position, depending on the excitation wavelength. The obtained data are listed in Tables S3 and S4. As the tables show, blue emission

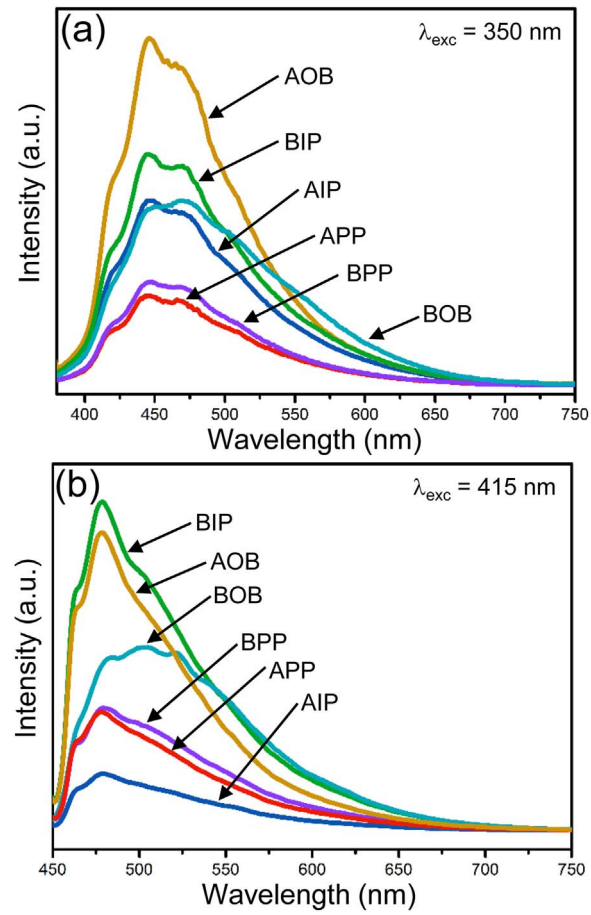

Fig. 8. Non-normalized PL spectra obtained at room temperature for SHA and Ca-dHA samples at an excitation wavelength of (a) 350 nm and (b) 415 nm.

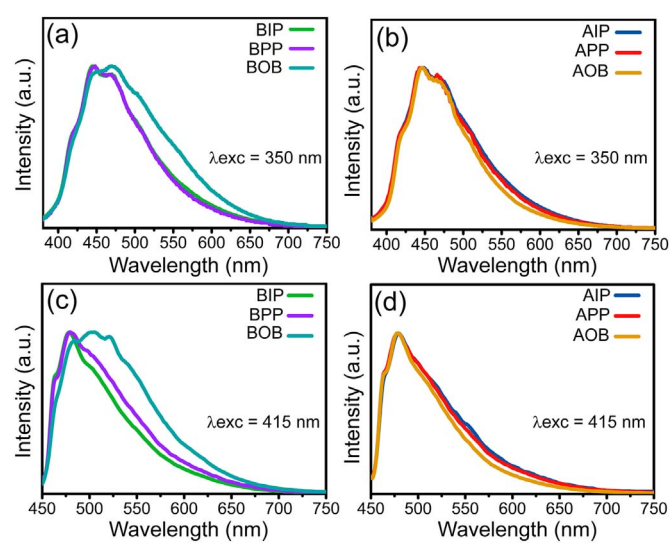

Fig. 9. Normalized PL spectra obtained at room temperature. SHA samples prepared in a basic environment and at an excitation wavelength of (a) λ_{exc} = 350 nm and (c) λ_{exc} = 415 nm. Ca-dHA samples prepared in an acidic environment and at an excitation wavelength of (b) λ_{exc} = 350 nm and (d) λ_{exc} = 415 nm.

centers, which occur at 467 and 475 nm for excitation at 350 and 415 nm, respectively, constitute high percentages of the area; the same holds true for green emission centers, which occur at 496 nm, for both excitation wavelengths. This confirms that the deep- and shallow-level defect states, located approximately in the middle and near to the CB,

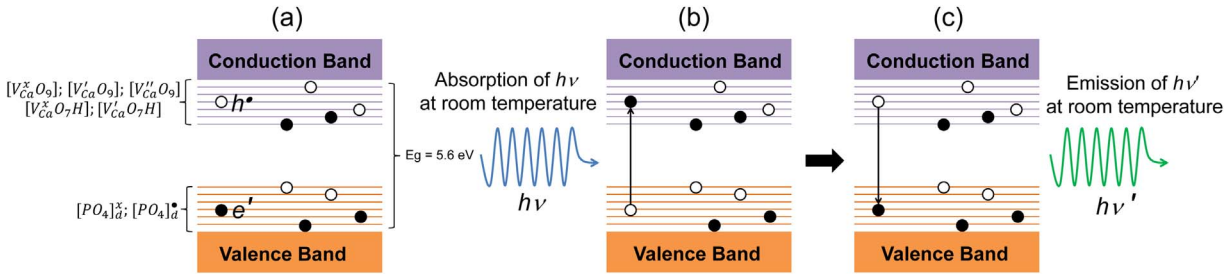

Fig. 10. (a) Schematic of band structures of SHA and Ca-dHA samples; (b) excitation process (formation of e'-$h^{\bullet}$ pairs) between intermediary energy levels; (c) recombination processes of e'-$h^{\bullet}$ pairs, which may result in PL emission ($h\nu > h\nu'$).

respectively, of the forbidden zone, contribute significantly to the electronic recombination mechanisms. The BOB sample excited at 415 nm, exhibited a different trend, i.e., in addition to the green component, the yellow also accounted for high percentages of the area. Therefore, deep energy levels within the band gap of this sample result mainly from the effect of surface and interface defects.

The surface and interface defects, distortions in $[PO_4]$ clusters, and ionic and interstitial V_{Ca} (found in both bulk and surface), can change the electronic structure of HA samples. Moreover, some surface states, which are intrinsic to the crystal termination or arising from crystalline surface defects, induce changes in the final physicochemical properties of any material [73]. A single crystal can be composed of various crystallographic planes with their respective surface energies [74]. These intrinsic surface energies play an important role in the formation and organization of localized empty and occupied energy states within the band gap [75].

Considering the UV–vis and PL results, we proposed a single-band structure model (see Fig. 10) to explain the PL behavior of our SHA and Ca-dHA samples. The central idea was mainly based on some papers published in the literature [32,61,63,68,69], and in the effect of structural order-disorder. In this model, the forbidden band gap consists of several empty and occupied intermediary energy levels, which arise from defects (bulk, surface, and interface) (Fig. 10(a)). We believe that the shallow levels near the CB edge are created mainly by V_{Ca}, which are associated with Ca *3p* and *4s* states. The deep levels and shallow levels near the VB edge are dominated by the states of the $[PO_4]$ clusters, i.e., P *3s, 3p* and O *2s, 2p* states, respectively. During the excitation process at room temperature, electrons located at low energy levels near the VB absorb the photon energies ($h\nu$) and, consequently, are promoted to intermediary energy levels near the CB (Fig. 10(b)). The energies arising from these electronic transitions are converted to photons ($h\nu'$) ($h\nu > h\nu'$) (radiative recombination) (Fig. 10(c)), when the electrons return to lower energy states. In addition, the broad and intense PL spectra of the HA samples are attributed to the numerous photons generated by electronic transitions, which involve various energy states. The transitions between very close energy levels may result in a non-radiative recombination process.

In future study, we will perform theoretical calculations based on these experimental data, in order to fully explain the present results.

4. Conclusions

Nano- and micro-particles of SHA and Ca-dHA were obtained via the chemical precipitation method, owing to the effectiveness of this synthetic route and the appropriate choice of experimental parameters (addition rate of the phosphate precursor and pH environment). The as-synthesized samples were characterized by means of ICP-AES, XRD, FTIR and Raman spectroscopies. The intense and well-defined diffraction peaks revealed that all HA samples have a structural periodicity at long-range, while the presence of structural order at short-range, i.e., clusters corresponding to the local coordination of Ca and P atoms, was confirmed via FTIR and Raman spectra. Moreover, there was a slight loss of resolution of the vibrational bands associated with $[PO_4]$ clusters in HA synthesized in a basic environment. These results can be associated to distortions in the structural order at short-range. In addition, bands corresponding to the vibrations associated with $[PO_4H]$ clusters, which are typically from Ca-dHA, occurred in both FTIR and Raman spectra of the samples synthesized in an acidic environment.

The particle size and shape (rods, needles, plates, and rices) varied with the addition rate of the phosphate precursor and the pH employed during the precipitation. The PL spectra of the as-prepared samples exhibited broad band profiles, and with maximum emissions located at the blue and green regions of the visible electromagnetic spectrum. Moreover, the SHA and Ca-dHA samples presented higher E_g (from 5.59 to 5.72 eV) than those corresponding to the excitation wavelengths (~ 3.54 and ~ 2.98 eV at 350 and 415 nm, respectively) used in the PL measurements. This behavior is attributed to the existence of a high density of intermediary energy levels (shallow and deep levels) in the forbidden band, owing to the presence of bulk, surface and interface defects.

Acknowledgment

The authors are grateful to the FAPESP (#2013/11144-3), FAPESP/CEPID (#2013/07296-2), CAPES/PNPD, and CNPq (#573636/2008-7), Universitat Jaume I (P1 1B2013-65 and UJIB-2016-38), and Ministerio de Economía y Competitividad (MAT2016-80410-P and Salvador Madariaga program PRX15/00261) for the financial support of this research. Special thanks to Mr. Rorivaldo Camargo for SEM measurements, Prof. Dr. Joaquim A. Nobrega and Dr. Alex Virgilio for ICP-AES analyses, and João Paulo de Campos da Costa by the graphic design.

Appendix A. Supplementary material

Supplementary data associated with this article can be found in the online version at http://dx.doi.org/10.1016/j.ceramint.2017.09.164.

References

[1] R.T. Wegh, H. Donker, K.D. Oskam, A. Meijerink, Visible quantum cutting in $LiGdF_4$:Eu^{3+} through downconversion, Science 283 (1999) 663–666.
[2] S. Nakamura, T. Mukai, M. Senoh, Candela-class high-brightness InGaN/AlGaN double-heterostructure blue-light-emitting diodes, Appl. Phys. Lett. 64 (1994) 1687–1689.
[3] S. Kunimi, S. Fujihara, Elaboration of blue-emitting blue pigments based on Eu^{2+}/Co^{2+} codoped $BaMgAl_{10}O_{17}$ through the heterogeneous distribution of dopants, Dyes Pigment. 91 (2011) 49–54.
[4] Y. Ma, S. Wang, L. Wang, Nanomaterials for luminescence detection of nitroaromatic explosives, Trends Anal. Chem. 65 (2015) 13–21.
[5] M. Bruchez Jr., M. Moronne, P. Gin, S. Weiss, A.P. Alivisatos, Semiconductor nanocrystals as fluorescent biological labels, Science 281 (1998) 2013–2016.
[6] N.J. Durr, T. Larson, D.K. Smith, B.A. Korgel, K. Sokolov, A. Ben-Yakar, Two-photon luminescence imaging of cancer cells using molecularly targeted gold nanorods, Nano Lett. 7 (2007) 941–945.
[7] R.J. Wiglusz, R. Pazik, A. Lukowiak, W. Strek, Synthesis, structure, and optical properties of LiEu(PO3)4 nanoparticles, Inorg. Chem. 50 (2011) 1321–1330.
[8] Y. Xue, Y. Du, J. Yan, Z. Liu, P.X. Ma, X. Chen, B. Lei, Monodisperse photoluminescent and highly biocompatible bioactive glass nanoparticles for controlled drug delivery and cell imaging, J. Mater. Chem. B 3 (2015) 3831–3839.
[9] Q. Guo, L. Liao, L. Mei, H. Liu, Color-tunable photoluminescence and energy

transfer properties of single-phase $Ba_{10}(PO_4)_6O:Eu^{2+}$, Mn^{2+} phosphors, J. Solid State Chem. 232 (2015) 102–107.
[10] G. Li, C. che Lin, Y. Wei, Z. Quan, Y. Tian, Y. Zhao, T.-S. Chan, J. Lin, Controllable Eu valence for photoluminescence tuning in apatite-typed phosphors by cation cosubstitution effect, Chem. Commun. 52 (2016) 7376–7379.
[11] H. Li, L. Mei, H. Liu, Y. Liu, L. Liao, R.V. Kumar, Growth mechanism of surfactant-free size-controlled luminescent hydroxyapatite nanocrystallites, Cryst. Growth Des. 17 (2017) 2809–2815.
[12] Y. Jiménez-Flores, M. Suárez-Quezada, J.B. Rojas-Trigos, L. Lartundo-Rojas, V. Suárez, A. Mantilla, Characterization of Tb-doped hydroxyapatite for biomedical applications: optical properties and energy band gap determination, J. Mater. Sci. 52 (2017) 9990–10000.
[13] B. Ma, S. Zhang, J. Qiu, J. Li, Y. Sang, H. Xia, H. Jiang, J. Claverie, H. Liu, Eu/Tb codoped spindle-shaped fluorinated hydroxyapatite nanoparticles for dual-color cell imaging, Nanoscale 8 (2016) 11580–11587.
[14] X. Zheng, M. Liu, J. Hui, D. Fan, H. Ma, X. Zhang, Y. Wang, Y. Wei, Ln^{3+}-doped hydroxyapatite nanocrystals: controllable synthesis and cell imaging, Phys. Chem. Chem. Phys. 17 (2015) 20301–20307.
[15] Z. Liu, Q. Wang, S. Yao, L. Yang, S. Yu, X. Feng, F. Li, Synthesis and characterization of Tb^{3+}/Gd^{3+} dual-doped multifunctional hydroxyapatite nanoparticles, Ceram. Int. 40 (2014) 2613–2617.
[16] R.J. Wiglusz, A. Kedziora, A. Lukowiak, W. Doroszkiewicz, W. Strek, Hydroxyapatites and europium(III) doped hydroxyapatites as a carrier of silver nanoparticles and their antimicrobial activity, J. Biomed. Nanotechnol. 8 (2012) 605–612.
[17] P. Yang, Z. Quan, C. Li, X. Kang, H. Lian, J. Lin, Bioactive, luminescent and mesoporous europium-doped hydroxyapatite as a drug carrier, Biomaterials 29 (2008) 4341–4347.
[18] A. Doat, M. Fanjul, F. Pellé, E. Hollande, A. Lebugle, Europium-doped bioapatite: a new photostable biological probe, internalizable by human cells, Biomaterials 24 (2003) 3365–3371.
[19] G.S. Kumar, E.K. Girija, Flower-like hydroxyapatite nanostructure obtained from eggshell: a candidate for biomedical applications, Ceram. Int. 39 (2013) 8293–8299.
[20] C. Wang, D. Liu, C. Zhang, J. Sun, W. Feng, X.-J. Liang, S. Wang, J. Zhang, Defect-related luminescent hydroxyapatite-enhanced osteogenic differentiation of bone mesenchymal stem cells via an ATP-induced cAMP/PKA pathway, ACS Appl. Mater. Interfaces 8 (2016) 11262–11271.
[21] K. Deshmukh, M.M. Shaik, S.R. Ramanan, M. Kowshik, Self-activated fluorescent hydroxyapatite nanoparticles: a promising agent for bioimaging and biolabeling, ACS Biomater. Sci. Eng. 2 (2016) 1257–1264.
[22] S.Y. Park, K.-I. Kim, S.P. Park, J.H. Lee, H.S. Jung, Aspartic acid-assisted synthesis of multifunctional strontium-substituted hydroxyapatite microspheres, Cryst. Growth Des. 16 (2016) 4318–4326.
[23] C. Zhang, C. Li, S. Huang, Z. Hou, Z. Cheng, P. Yang, C. Peng, J. Lin, Self-activated luminescent and mesoporous strontium hydroxyapatite nanorods for drug delivery, Biomaterials 31 (2010) 3374–3383.
[24] C. Zhang, S. Huang, D. Yang, X. Kang, M. Shang, C. Peng, J. Lin, Tunable luminescence in Ce^{3+}, Mn^{2+}-codoped calcium fluorapatite through combining emissions and modulation of excitation: a novel strategy to white light emission, J. Mater. Chem. 20 (2010) 6674–6680.
[25] K. Sudarsanan, R.A. Young, Significant precision in crystal structural details: holly springs hydroxyapatite, Acta Crystallogr. B25 (1969) 1534–1543.
[26] X. Lijuan, J. Liuyun, X. Chengdong, J. Lixin, Effect of different synthesis conditions on the microstructure, crystallinity and solubility of Mg-substituted hydroxyapatite nanopowder, Adv. Powder Technol. 25 (2014) 1142–1146.
[27] H. Tanaka, A. Ohnishi, Synthesis of Ti(IV)-substituted calcium hydroxyapatite microparticles by hydrolysis of phenyl phosphates, Adv. Powder Technol. 24 (2013) 1028–1033.
[28] V. Uskoković, The role of hydroxyl channel in defining selected physicochemical peculiarities exhibited by hydroxyapatite, RSC Adv. 5 (2015) 36614–36633.
[29] R.M. Wilson, J.C. Elliott, S.E.P. Dowker, L.M. Rodriguez-Lorenzo, Rietveld refinements and spectroscopic studies of the structure of Ca-deficient apatite, Biomaterials 26 (2005) 1317–1327.
[30] J.C. Elliot, Structure and Chemistry of the Apatites and Other Calcium Orthophosphates, Elsevier, Amsterdam, 1994.
[31] S.S. Bhat, U.V. Waghmare, U. Ramamurty, First-principles study of structure, vibrational, and elastic properties of stoichiometric and calcium-deficient hydroxyapatite, Cryst. Growth Des. 14 (2014) 3131–3141.
[32] A.V. Bystrova, Y.D. Dekhtyar, A.I. Popov, J. Coutinho, V.S. Bystrov, Modified hydroxyapatite structure and properties: modeling and synchrotron data analysis of modified hydroxyapatite structure, Ferroelectrics 475 (2015) 135–147.
[33] C. Zhang, J. Yang, Z. Quan, P. Yang, C. Li, Z. Hou, J. Lin, Hydroxyapatite nano- and microcrystals with multiform morphologies: controllable synthesis and luminescence properties, Cryst. Growth Des. 9 (2009) 2725–2733.
[34] M. Sadat-Shojai, M.-T. Khorasani, E. Dinpanah-Khoshdargi, A. Jamshidi, Synthesis methods for nanosized hydroxyapatite with diverse structures, Acta Biomater. 9 (2013) 7591–7621.
[35] T.R. Machado, J.C. Sczancoski, H. Beltrán-Mir, I.C. Nogueira, M.S. Li, J. Andrés, E. Cordoncillo, E. Longo, A novel approach to obtain highly intense self-activated photoluminescence emissions in hydroxyapatite nanoparticles, J. Solid State Chem. 249 (2017) 64–69.
[36] C. Suryanarayana, M.G. Norton, X-Ray Diffraction: A Practical Approach, Plenum Press, New York, 1998.
[37] K. Tomoda, H. Ariizumi, T. Nakaji, K. Makino, Hydroxyapatite particles as drug carriers for proteins, Colloids Surf. B Biointerfaces 76 (2010) 226–235.
[38] S.V. Dorozhkin, Calcium orthophosphate bioceramics, Ceram. Int. (2015) 1–54.
[39] V. Uskoković, D.P. Uskoković, Nanosized hydroxyapatite and other calcium phosphates: chemistry of formation and application as drug and gene delivery agents, J. Biomed. Mater. Res. B Appl. Biomater. 96B (2011) 152–191.
[40] A.R. West, Basic Solid State Chemistry, John Wiley & Sons, Chichester, 1999.
[41] B.O. Fowler, Infrared studies of apatites. I. Vibrational assignments for calcium, strontium, and barium hydroxyapatites utilizing isotopic substitution, Inorg. Chem. 13 (1974) 194–207.
[42] M. Corno, C. Busco, B. Civalleri, P. Ugliengo, Periodic *ab initio* study of structural and vibrational features of hexagonal hydroxyapatite $Ca_{10}(PO_4)_6(OH)_2$, Phys. Chem. Chem. Phys. 8 (2006) 2464–2472.
[43] Y. Leung, M.A. Walter, R.Z. LeGeros, Second derivative infrared spectra of hydroxyapatite, Spectrochim. Acta 46A (1990) 1453–1459.
[44] G. Penel, G. Leroy, C. Rey, E. Bres, MicroRaman spectral study of the PO_4 and CO_3 vibrational modes in synthetic and biological apatites, Calcif. Tissue Int. 63 (1998) 475–481.
[45] A. Antonakos, E. Liarokapis, T. Leventouri, Micro-Raman and FTIR studies of synthetic and natural apatites, Biomaterials 28 (2007) 3043–3054.
[46] J.D. Pasteris, B. Wopenka, J.J. Freeman, K. Rogers, E. Valsami-Jones, J.A.M. van der Houwen, M.J. Silva, Lack of OH in nanocrystalline apatite as a function of degree of atomic order: implications for bone and biomaterials, Biomaterials 25 (2004) 229–238.
[47] B.O. Fowler, M. Markovic, W.E. Brown, Octacalcium phosphate. 3. Infrared and raman vibrational spectra, Chem. Mater. 5 (1993) 1417–1423.
[48] M.J.J.M. Van Kemenade, P.L. De Bruyn, A kinetic study of precipitation from supersaturated calcium phosphate solutions, J. Colloid Interface Sci. 118 (1987) 564–585.
[49] L.M. Rodríguez-Lorenzo, M. Vallet-Regí, Controlled crystallization of calcium phosphate apatites, Chem. Mater. 12 (2000) 2460–2465.
[50] C. Liu, Y. Huang, W. Shen, J. Cui, Kinetics of hydroxyapatite precipitation at pH 10 to 11, Biomaterials 22 (2001) 301–306.
[51] B. Liu, H.C. Zeng, Symmetric and asymmetric Ostwald ripening in the fabrication of homogeneous core-shell semiconductors, Small 1 (2005) 566–571.
[52] H. Chen, B.H. Clarkson, K. Sun, J.F. Mansfield, Self-assembly of synthetic hydroxyapatite nanorods into an enamel prism-like structure, J. Colloid Interface Sci. 288 (2005) 97–103.
[53] J.D. Chen, Y.J. Wang, K. Wei, S.H. Zhang, X.T. Shi, Self-organization of hydroxyapatite nanorods through oriented attachment, Biomaterials 28 (2007) 2275–2280.
[54] F.-Z. Cui, J. Ge, New observations of the hierarchical structure of human enamel, from nanoscale to microscale, J. Tissue Eng. Regen. Med. 1 (2007) 185–191.
[55] J. Zhan, Y.-H. Tseng, J.C.C. Chan, C.-Y. Mou, Biomimetic formation of hydroxyapatite nanorods by a single-crystal-to-single-crystal transformation, Adv. Funct. Mater. 15 (2005) 2005–2010.
[56] W.E. Brown, J.P. Smith, J.R. Lehr, A.W. Frazier, Crystallographic and chemical relations between octacalcium phosphate and hydroxyapatite, Nature 196 (1962) 1050–1055.
[57] R.A. Terpstra, P. Bennema, Crystal morphology of octacalcium phosphate: theory and observation, J. Cryst. Growth 82 (1987) 416–426.
[58] J.L. Lyons, A. Janotti, C.G. de Walle, Shallow versus deep nature of Mg acceptors in nitride semiconductors, Phys. Rev. Lett. 108 (2012) 156403.
[59] D. Haranath, V. Shanker, D.R. Vij, Handbook of Electroluminescent Materials, Taylor & Francis, London, 2004.
[60] G. Botelho, J.C. Sczancoski, J. Andres, L. Gracia, E. Longo, Experimental and theoretical study on the structure, optical properties, and growth of metallic silver nanostructures in Ag_3PO_4, J. Phys. Chem. C 119 (2015) 6293–6306.
[61] K. Matsunaga, A. Kuwabara, First-principles study of vacancy formation in hydroxyapatite, Phys. Rev. B 75 (2007) 14102.
[62] E.E. Jay, P.M. Mallinson, S.K. Fong, B.L. Metcalfe, R.W. Grimes, Divalent cation diffusion in calcium fluorapatite, J. Mater. Sci. 46 (2011) 7459–7465.
[63] V.S. Bystrov, J. Coutinho, A.V. Bystrova, Y.D. Dekhtyar, R.C. Pullar, A. Poronin, E. Palcevskis, A. Dindune, B. Alkan, C. Durucan, E.V. Paramonova, Computational study of hydroxyapatite structures, properties and defects, J. Phys. D. Appl. Phys. 48 (2015) 195302.
[64] F.A. Kröger, H.J. Vink, Relations between the concentrations of imperfections in crystalline solids, Solid State Phys. 3 (1956) 307–435.
[65] A.F. Gouveia, J.C. Sczancoski, M.M. Ferrer, A.S. Lima, M.R.M.C. Santos, M.S. Li, R.S. Santos, E. Longo, L.S. Cavalcante, Experimental and theoretical investigations of electronic structure and photoluminescence properties of β-Ag_2MoO_4 microcrystals, Inorg. Chem. 53 (2014) 5589–5599.
[66] A. Salleo, Organic Electronics: Emerging Concepts and Technologies, Wiley-VHC, Weinheim, 2013.
[67] L. Tolvaj, K. Mitsui, D. Varga, Validity limits of Kubelka-Munk theory for DRIFT spectra of photodegraded solid wood, Wood Sci. Technol. 45 (2011) 135–146.
[68] A. Slepko, A.A. Demkov, First-principles study of the biomineral hydroxyapatite, Phys. Rev. B 84 (2011) 134108.
[69] G. Rosenman, D. Aronov, L. Oster, J. Haddad, G. Mezinskis, I. Pavlovska, M. Chaikina, A. Karlov, Photoluminescence and surface photovoltage spectroscopy studies of hydroxyapatite nano-bio-ceramics, J. Lumin 122–123 (2007) 936–938.
[70] M.D. McCluskey, E.E. Haller, Dopants and Defects in Semiconductors, Taylor & Francis, London, 2012.
[71] V.M. Longo, L.S. Cavalcante, A.T. de Figueiredo, L.P.S. Santos, E. Longo, J.A. Varela, J.R. Sambrano, C.A. Paskocimas, F.S. De Vicente, A.C. Hernandes, Highly intense violet-blue light emission at room temperature in structurally disordered $SrZrO_3$ powders, Appl. Phys. Lett. 90 (2007) 91906.
[72] R.L. Penn, J.F. Banfield, Imperfect oriented attachment: dislocation generation in defect-free nanocrystals, Science 281 (1998) 969–971.
[73] L.J. Brillson, Surfaces and Interfaces of Electronic Materials, Wiley-VHC, Weinheim, 2012.
[74] R. György, P.B. Barna, Materials Surface Processing by Direct Energy Techniques, Elsevier, Amsterdam, 2006.
[75] S. Rein, Lifetime Spectroscopy: A Method of Defect Characterization in Silicon Photovoltaic Applications, Springer-Verlag Berlin Heidelberg, Tokyo, 2006.